Received: 20 April 2022 | Revised: 21 June 2022 | Accepted: 28 July 2022

DOI: 10.1002/suco.202200387

ARTICLE

Three-dimensional testing of fasteners

Dustin Konertz[1] | Christoph Mahrenholtz[2] | Peter Mark[1]

[1]Institute of Concrete Structures, Ruhr University Bochum, Bochum, Germany

[2]Jordahl GmbH, Berlin, Germany

Correspondence
Dustin Konertz, Ruhr University Bochum, Institute of Concrete Structures, Universitätstr. 150, 44801 Bochum, Germany.
Email: dustin.konertz@rub.de

Abstract

Experimental results of tests to investigate the load-bearing behavior of anchor channels embedded in concrete and subjected to loads in three-dimensional (3D) interaction are presented. For testing, a variably adjustable rig is introduced in which arbitrary 3D loads are applied with just one hydraulic cylinder. Investigations focus on concrete failure. The test program includes variable load angles and anchor channels installed at the edges and at corner of concrete prisms. In both configurations a significant impact of the loading direction regarding the channel axis is found. Mathematically interaction is captured with trilinear and Lamè curves. Therein, the experimental findings are reflected by individual model parameters that yield the best fit in regression. For both configurations, an optimal prognosis model is derived which covers all 3D load situations in assured quality. Moreover, the tests prove the general suitability of the developed rig, which thus qualifies for application in other experimental settings.

KEYWORDS

anchor channels, fasteners, load bearing behavior, load interaction, three-dimensional testing

1 | INTRODUCTION

Fasteners are used to connect components or elements of the technical building equipment with concrete elements. Just as dowels or anchor plates, anchor channels are widely used.[1] They are characterized by a comparatively high load capacity and allow a variable fastening position along the channel axis. Special toothed channels allow not only tensile and transverse stressing but also stressing in the longitudinal direction of the channel. Due to this advantage, anchor channels are frequently used for attaching pipelines, catenary wires and installations in tunnel construction as well as guiding racks in elevator construction. A further field of application is the attaching of curtain walls, as for example in the world's tallest building, the Burj Khalifa in Dubai (Figure 1).[2,3] Due to the sometimes extreme conditions at great heights, three-dimensional (3D) stressing of the anchor channel must be expected here. In addition to the vertical load due to self-weight of the façade (V), tensile loads (N) are introduced into the channel due to wind (Figure 1, left). Horizontal loads (H), which cannot generally be neglected, occur due to wind as well as due to constraints, for example, induced by temperature.

If all these components act simultaneously in 3D loading, interaction occurs that must carefully be taken into account when assessing the ultimate bearing capacity.[5] In

Discussion on this paper must be submitted within two months of the print publication. The discussion will then be published in print, along with the authors' closure, if any, approximately nine months after the print publication.

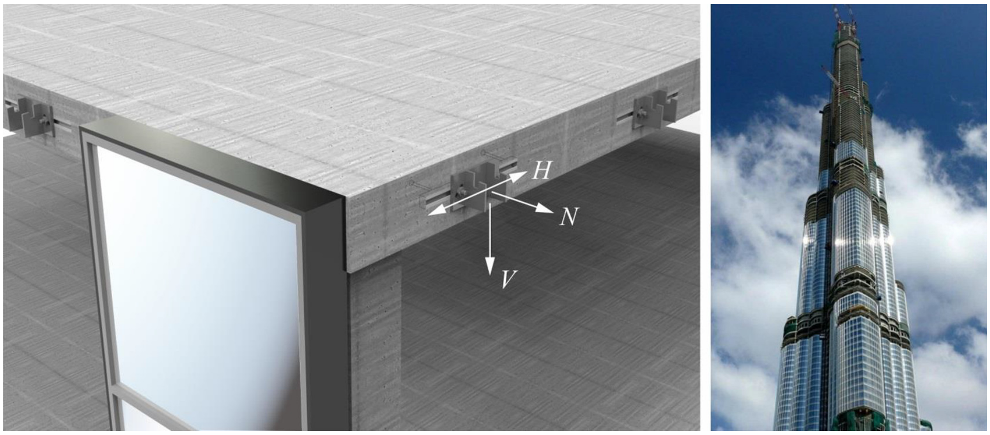

FIGURE 1 Attachment of a curtain wall using anchor channels on the example of the Burj Khalifa[4]

addition to research focused on the main directions (H, N, V)[6,7,8,9,10] two-dimensional (2D) interaction has already been investigated, too. For example, Oluokon and Burdette[11] dealt with the load-bearing behavior of anchor channels at the edge of thin concrete plates under combined tensile and transverse loads. Their 2D tests served to highlight interaction in case of concrete failure. The test-setup combined two hydraulic jacks for load application. At first, a horizontal load was applied and then kept constant, while the vertical component was successively increased. Consequently, the angle of the test load changed continuously during their experiment. Thus, the time of failure and the associated combination of the two components was initially unknown and had to be determined from the test retrospectively.

Wohlfahrt's investigations have also treated, among other things, concrete failure due to interaction of tensile and transverse loads.[8] His test-setup employed a steel frame that was supported against the specimen and in which the load was applied through a jack that could be fixed at certain angles. That way, the load-bearing behavior of anchor channels could be investigated at predefined angles.

Both studies have yielded similar equations to describe the 2D interaction, with trilinear or elliptical curves. In these forms, they have also found their way into standardization such as ACI 318,[12] EN 1992-4,[13] and others.[14–17]

However, up to now no study has been published to the authors' knowledge that deals with interaction of tensile and/or transverse with longitudinal loads and the resulting 3D stresses. This is exactly where our work starts from. We focus on the investigation of spatial interaction and its influence on the ultimate bearing capacity in case of concrete failure. Key is a test rig called "3D tester" that has been newly developed to strictly separate load application from retention of the specimen. It allows for arbitrary geometries and arrangements of fasteners in the specimen and provides sufficient space for forming and placement of specimens. Despite all variability arbitrary spatial angles can be fixed for load inclination. With this test rig a comprehensive test series of two- and three-dimensionally loaded anchor channels has been performed to study interaction effects and to derive an optimal prognosis model for practical application.

2 | TEST SERIES AND PERFORMANCE REQUIREMENTS FOR 3D TESTER

Prior to the development of the 3D tester the test series was defined to work out all experimental requirements and match it with the test-setup. To ensure concrete failure in all experiments dimensioning of the specimen and positioning of the anchor channel are utmost decisive. A further challenge is to make the specimen small to minimize the effort during casting and testing.

2.1 | Materials

For that purpose a short piece with a single anchor was cut from an arbitrary long serrated anchor channel. The cut-off is interpreted as a representative end section, whose dimensions can be taken from Figure 2. The advantage to investigate this short substitute instead of a channel with several anchors is that then the expected break-out body and the required dimension of the specimens are much smaller and free from undesired mutual interference of different anchors.[18] Moreover no distribution neither of the tensile,[10] transverse,[19] nor longitudinal forces[20–23] to other anchors occurs during load application. Thus, the true force on an anchor and the channel around can clearly be investigated and understood. The length of the anchor that yields the anchoring depth h_{ef} is comparatively small in order to ensure concrete failure even under tensile stress.

The utilized concrete is characterized by a maximum grain size of 16 mm (0/2: 44%, 2/8: 20%, 8/16: 36%) and a water to cement ratio of 0.6 (CEM II/A 42.5 N). After concreting, the concrete was covered with foil, kept moist and stored at 21°C, and after 3 days at the earliest, the formwork was removed. The strength of the specimen in the two series was in between 26.7 and 30.8 N/mm^2; on average 27.6 N/mm^2. The concrete age on the first day of testing was 13 days in series I and 12 days in series II. For each series concrete of one batch was used. The strength of the concrete was deliberately not chosen to be higher, as otherwise steel failure (e.g., channel lip or bolt) could have occurred.

2.2 | Test specimen design

The experimental program comprised 2D load interaction tests of anchor channels close to an edge (E) and 3D investigations at a corner (C). The specimen for the edge configuration differ with respect to placement as well as loading in transverse (T) and longitudinal direction (L). Thus, in ET-tests interaction of tensile and transverse loading is observed, while EL-tests monitor interaction of tensile and longitudinal loadings. C-tests enable to study 3D tensile interaction, finally.

Figure 3 displays the different configurations along with the horizontal (α) and vertical load angles (β) and the edge distances c_1 and c_2. For convenience, all configurations are denoted uniquely throughout the paper as follows: *Conf.*-α–β. Herein, *Conf.* denotes the type of configuration with up to two capital letters while the two figures indicate the angle of the horizontal loading direction (α) and subsequently the angle of the vertical direction (β) (see Figure 3).

The size of the specimens directly depends on the edge distances since these determine the size of the breakout body. The two distances c_1 and c_2 according to Figure 3 run from the perpendicular edges to the anchor's axis.

The bracing required in the experiment to fix the specimen is placed asides the expected breakout body of the anchor channel to avoid any impact on the result. Figure 4 indicates the regions to be kept free and those used for the bracings. The projection of the breakout body on the surface is rotationally symmetric due to tensile loading. The radius of the circle is obtained from Equation (1) according to EN 1992-4[13]:

$$R = \left(2.8 - 1.3 \cdot \frac{h_{ef}}{180}\right) \cdot h_{ef} = 185\,\mathrm{mm} \tag{1}$$

The size of the breakout body due to transverse or longitudinal stressing is defined by the height h_{cr} and the width b_{cr} (cr: crack) with respect to the edges. Since the breakout body is assumed to be symmetric with respect

b_{ch}	(mm)	53.0
h_{ch}	(mm)	34.0
l	(mm)	85.0
l_1	(mm)	50.0
l_2	(mm)	35.0
h_{ef}	(mm)	85.0
d_1	(mm)	14.0
d_2	(mm)	28.0

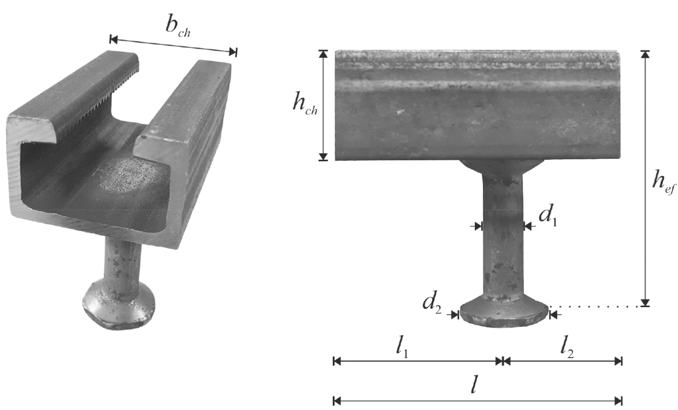

FIGURE 2 Nominal dimensions of the serrated anchor channel tested

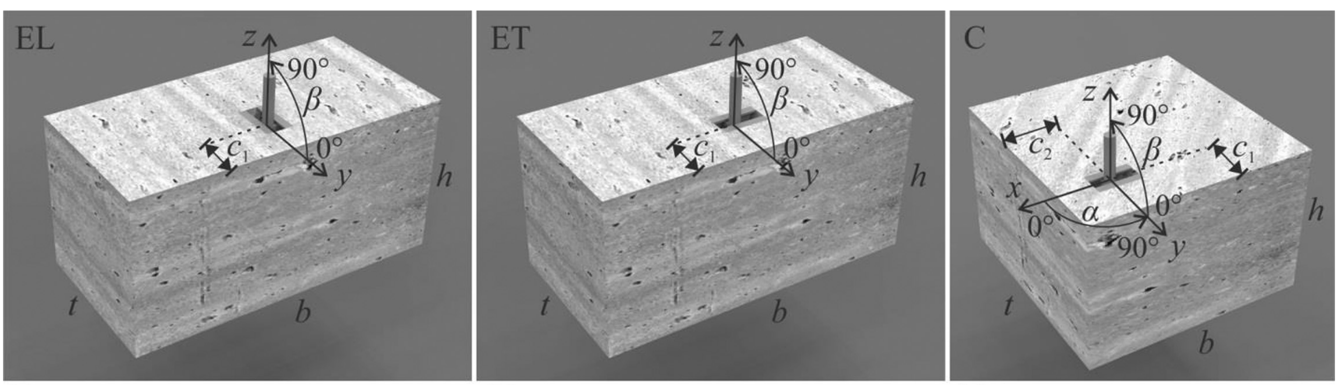

(a) (b) (c)

FIGURE 3 Test bodies and load directions with (a) longitudinal and (b) transverse channel orientation in edge configurations and (c) corner configurations

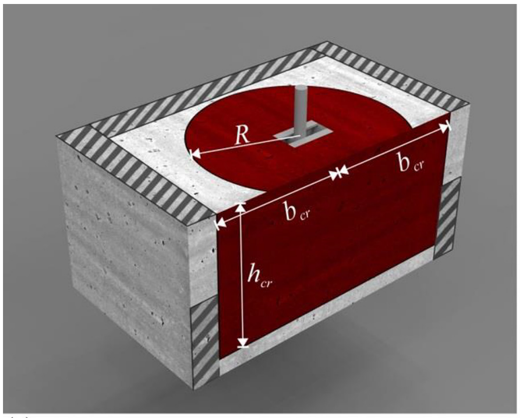

(a)

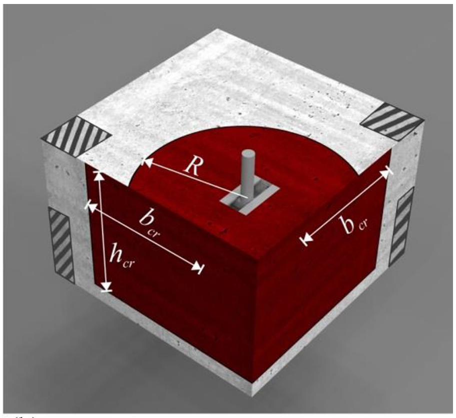

(b)

FIGURE 4 Maximum extent of the assumable breakout bodies (red; top area for tension, side area for shear) along with bracing regions (hatched) for (a) edge and (b) corner configurations

TABLE 1 Specifications of the specimens and tested load directions

Test configuration	Height h (mm)	Width b (mm)	Depth t (mm)	Edge distance c_1 (mm)	Edge distance c_2 (mm)	Load directions α (°)	Load directions β (°)
EL	300	600	350	100	100	90	0, 22.5, 45, 67.5, 90
ET	300	600	350	100	100	90	0, 22.5, 45, 67.5, 90
C	300	450	450	100	100	0, 22.5, 45, 67.5, 90	0, 22.5, 45, 67.5, 90

Abbreviations: C, corner configuration; EL, edge configuration—longitudinal loading; ET, edge configuration—transverse shear loading.

to the anchor, the width along the edges has to be kept free in both directions (Figure 4a). The minimum distances are computed from Equations (2) and (3) according to EN 1992-4[13] and EOTA,[24] as follows:

$$h_{cr} = 2c_1 + 2h_{ch} = 268\,\text{mm} \tag{2}$$

$$b_{cr} = 2.5c_1 = 250\,\text{mm} \tag{3}$$

The two distances are valid for the whole test program and computed from Equations (2) and (3) employing the parameters defined in Table 1 and Figure 2.

2.3 | Test program

Typical edge distances (c_1 and c_2) of 100 mm were specified for the test program. From the previously found regions, which are to be kept free, the specimen geometries can be derived by adding the necessary space for bracing (Table 1).

The interval of interesting load angles β runs from 0° (horizontal) to 90° (vertical). To capture 3D loadings in the corner configuration the angle α varies in the limits of 0° to 90°, too. Just then concrete breakout can be expected in that region (cf. Figure 3). All tests listed in Table 1 are obtained by equidistant splitting of the associated angles in the corner (C) and edge (EL and ET) configurations. For each configuration, two repetitions were planned and performed. But, in case of large deviations further tests were added. After the first series, however, it was found that for corner configurations with $\beta = 67.5°$ there was no relevant difference between them, so that two tests were skipped. The associated values were interpolated instead. Figure 5 visualizes the total test program with all configurations and shows the number of tests.

2.4 | Loading and measurement

In the experiment loading was applied via a prestressed screw (M20) placed in the channel directly above the anchor. This screw was prestressed with 350 Nm and fixed the flap of a steel construction for load application flexible.[25] This steel construction was connected to the cylinder and applied tension to the specimen (Figures 6 and 8). Between the flap and the anchor channel or the concrete surface a sheeting made of polytetrafluoroethylene (PTFE) was placed to minimize friction.[26,27]

Loading was applied path-controlled with a constant increase of 1 mm/min. During the experiment force and path of the cylinder as well as horizontal and vertical deflections of the screw were recorded.[28] The load cell

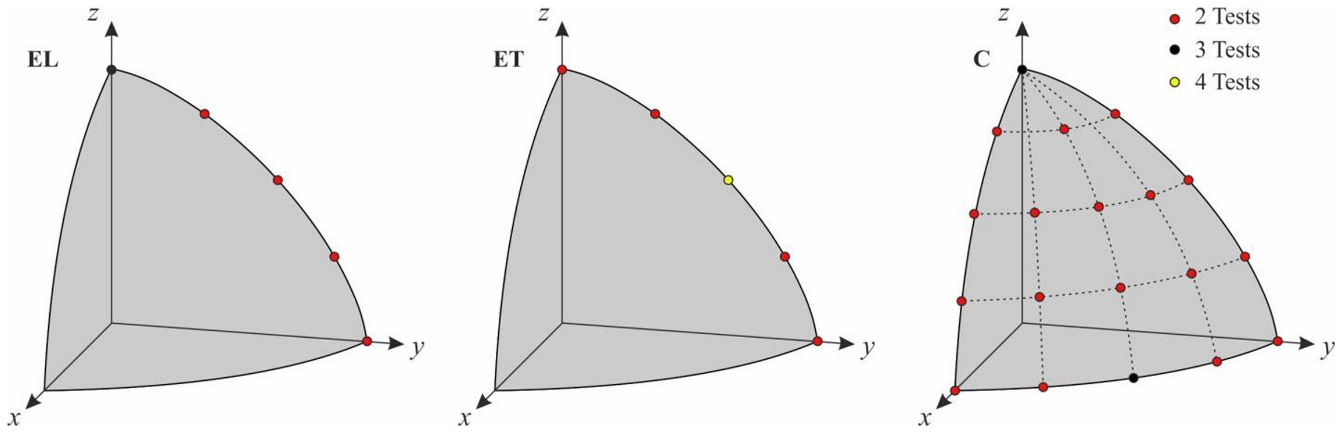

FIGURE 5 Visualization of the entire test program with the number of tests to be performed per configuration

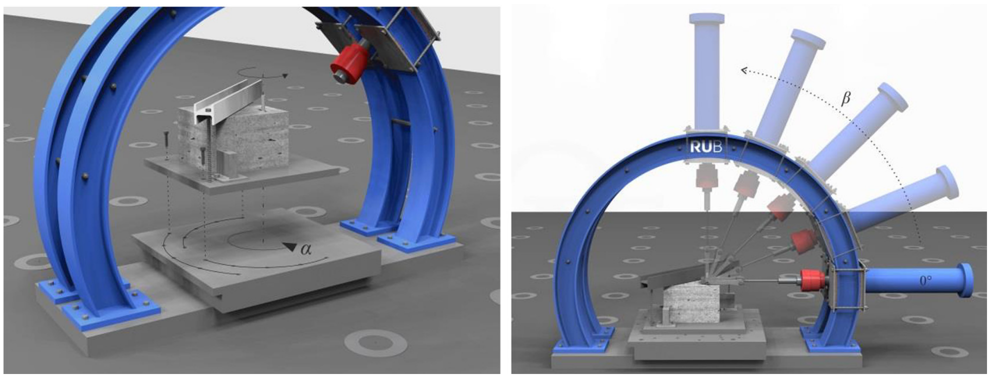

FIGURE 6 Horizontal rotation of the test body (α) and vertical rotation of the hydraulic cylinder (β)

was placed in front of the hydraulic cylinder and the inductive displacement transducers were placed at the top of the screw (vertical) and the side surface of the steel plate (horizontal) (Figure 8).

The maximum possible test loads differ dependent on the loading direction and lie between 70 and 120 kN. They correspond to the maximum bearing capacity of anchor or anchor channel and thus characterize steel failure. However, the specimens are designed so that concrete failure definitively happens first. Thus, lower maximum load levels are expected in the experiments.

3 | DESIGN OF THE 3D TESTER

3.1 | Construction and funtionality

For the execution of the experimental program described above, a variable 3D test rig (3D tester) was developed, taking into account all necessary boundary conditions. The fundamental idea was to build the test rig so that arbitrary 3D load directions can be generated combining horizontal and vertical angles (Figure 6). Inspired by the long established geographic positioning principle employing longitude and latitude the spatial loading direction can be described by a horizontal (α) and a vertical angle (β) (cf. Figure 5, right).

A specific challenge of the test rig lies in the variable position of the jack. The jack must be easy to fix and release and, at the same time, precisely orientated. Usually, only fixed positions of jacks are accepted in complex loading tests, like in tests of segmental linings[29] or of beams under bi-axial bending and shear.[30]

Practical implementation is achieved through a closed steel framework. Therein, the specimen is located at the center of a circular arc. More precisely, two arc-sections made from rolled structural steel run in parallel. For spatial stiffening both are rigidly connected in compression and tension several times. To the ground the arc-sections are also rigidly fixed via welded-on head plates that are screwed to the base plate on which the specimen is clamped. In between these two a loading jack is mounted, so that load application on the specimen happens from the outside.

All in all, a closed system is formed whose components can be adjusted independently of each other. The vertical loading angle β can be adjusted continuously placing the hydraulic jack along the arc section (Figure 6, right). The horizontal loading angle α is regulated by the orientation of a steel plate on which the specimen is fixed. For that purpose, this steel plate can be rotated around its central axis that is simultaneously the center of load application. Finally it is screwed via a bolt circle to the base plate. With angles α up to 360° and β up to 180°, this test rig offers even more variability than required for the experimental program at hand.

Its design ensures that the load is always applied at the center of the circle, where the load introduction to the anchor channel must be placed.

3.2 | Loads and dimensioning

The most decisive component of the test rig and the most challenging regarding its design are the arc-sections that are subjected to combined axial and shear forces as well as to a bending moment due to asymmetrical stressing by the jack in certain positions. Besides the mandatory stress limits of the steel cross-section, deformation must be limited to ensure that the line of action of the load introduction is not impaired.

A big challenge regarding the choice of the steel profile was with conflicting demands: On the one hand to keep the bending radius as small as possible to keep the test rig manageable and on the other hand ensuring preferably big stress reserves regarding maximum capacity. A choice of a bigger and thus stiffer profile would not automatically yield greater capacity reserves since the simultaneously rising minimum bending radius would induce higher moments and forces (M, N, Q) due to the same loading. Thus, a comparatively higher capacity of the profile in absolute would be relativized in relation. Iteration considering both demands has led to the compromise of a profile HEB 180. Indeed, the realized radius is the smallest one possible (Table 2).

For dimensioning, the maximum load of the hydraulic jack of 160 kN was used. With this load in the most unfavorable load position the cross-section of the profile is utilized to about 30%. This comes along with small deflections of 1.4 mm merely in direction of the line of action. Thus, they do not impair the loading angle much and are seen uncritical.

TABLE 2 Dimensions of the arches (steel frames)

Profile type	[–]	HEB 180
Inner diameter	[m]	2.04
Outer diameter	[m]	2.40
Circular segment	[°]	230
Central point[a]	[m]	0.5
Clear distance between	[m]	0.2

[a]Height over ground including head plates.

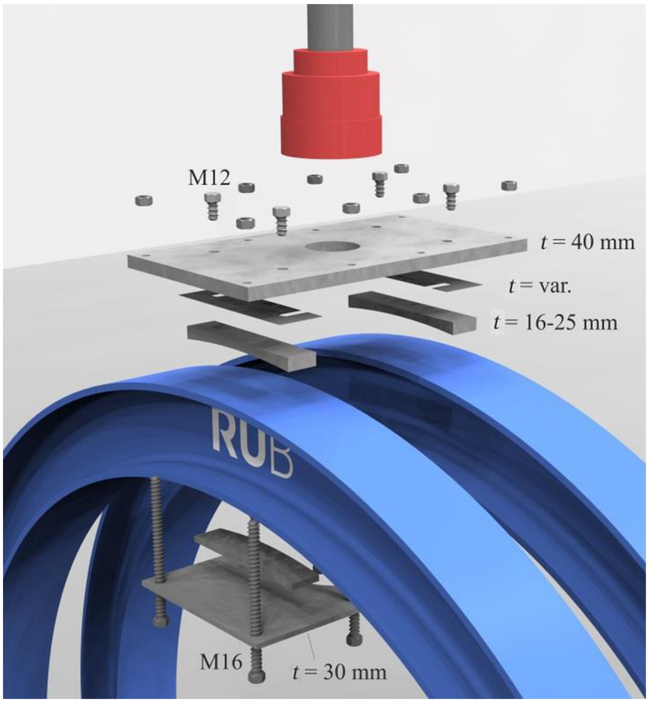

FIGURE 7 Mounting plates for installing the hydraulic jack

Please note that the changes in the cross-section and material properties that occur as a result of plastic deformation are not covered by the design. However, due to its low utilization the design is nevertheless considered sufficiently safe.

By contrast, all other components and connections such as head plates, screws, welding joints and the construction for load introduction are designed for higher loads.

3.3 | Components, details, and assembly

Besides the main component, the circular arc-sections discussed above, further components were developed, too. An important detail was the connection of the hydraulic jack via a braced plate for load induction with countered plates (Figure 7). The curvature of the arcs was compensated by calottes. Dimensional deviations between the arches were compensated by lining sheets that were slotted to enable a-posteriori installation with already mounted calottes.

The space inside the arc-sections defines the maximum acceptable dimensions of a specimen. Its maximum width is limited to the distance of the two base points of the arcs of 1.80 m. Its maximum height for arbitrary inclined loads coincides with the height of load induction in the center of the circular arc. It lies 0.50 m above the ground plate. In case of purely tensile loads (in vertical direction) even higher specimens can be tested since then the line of action is perpendicular to the ground plate

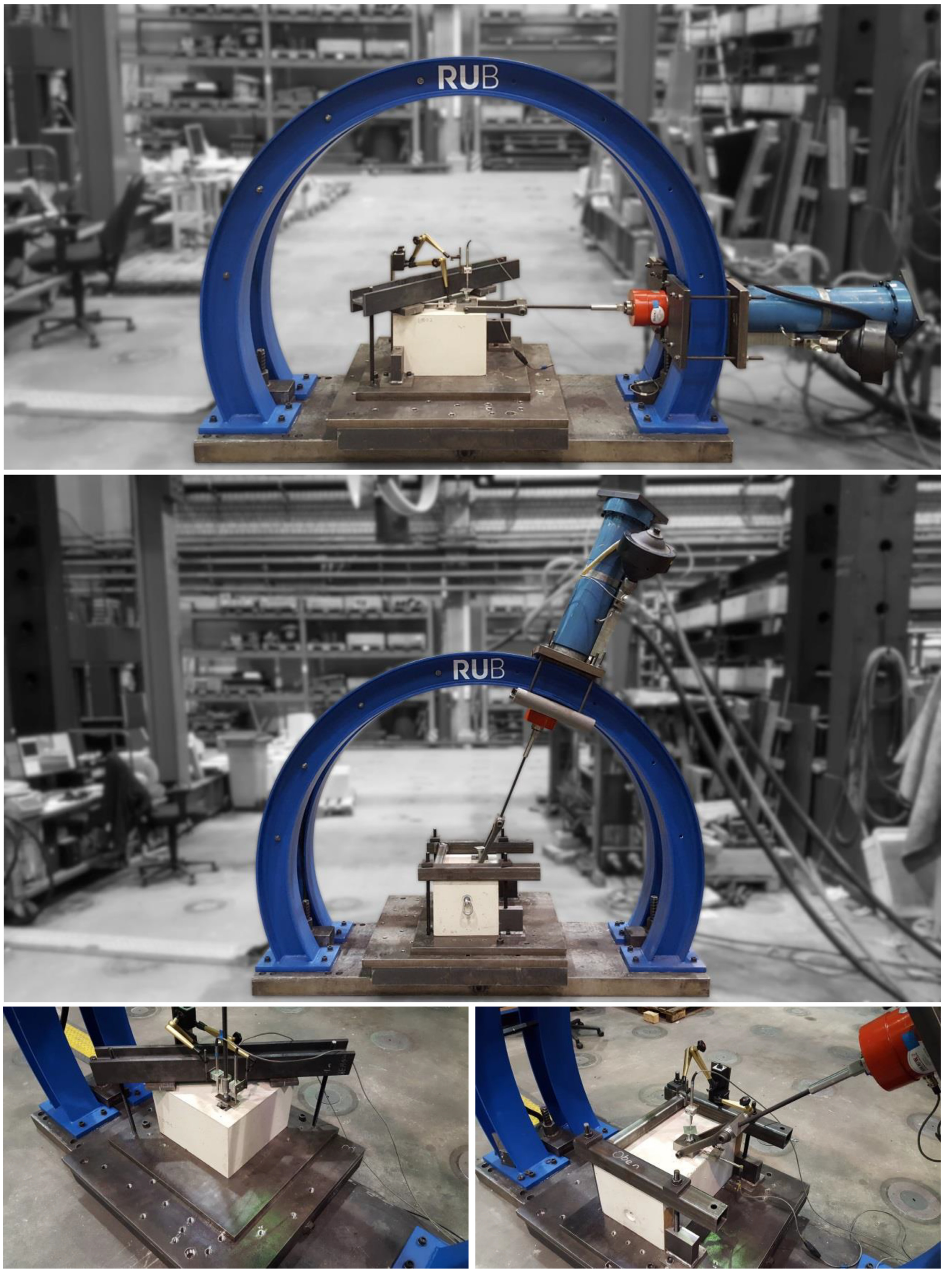

FIGURE 8 Three-dimensional tester: Final setup for configurations C-90-0 (top) and ET-90-67.5 (middle); details of specimen, bracing, and displacement transducers in corner and edge configuration (bottom)

($\beta = 90°$) and runs necessarily through the point of load induction at the bolt. For smaller specimen with $h < 0.50$ m lining sheets become necessary for leveling. The length of any specimen perpendicular to the arcs' plane is unrestricted. Figure 8 exemplifies the final setup in case of the anchor channel tests.

4 | TEST RESULTS

With this highly variable 3D tester the scheduled experimental program could completely be performed. As intended in all tests concrete failure occurred. Thus, 3D interaction is comprehensively captured and fully describable.

4.1 | Failure types

Figures 9 and 10 show the failure modes for 2D and 3D interaction. The fracture patterns differ for different loading angles. With flat vertical angles β concrete merely cracks on the side faces. The observed failure can be described as concrete edge failure. Steeper vertical angles crack the top surface. Since the cracks occur in a cone shape, this is usually described as concrete cone failure.

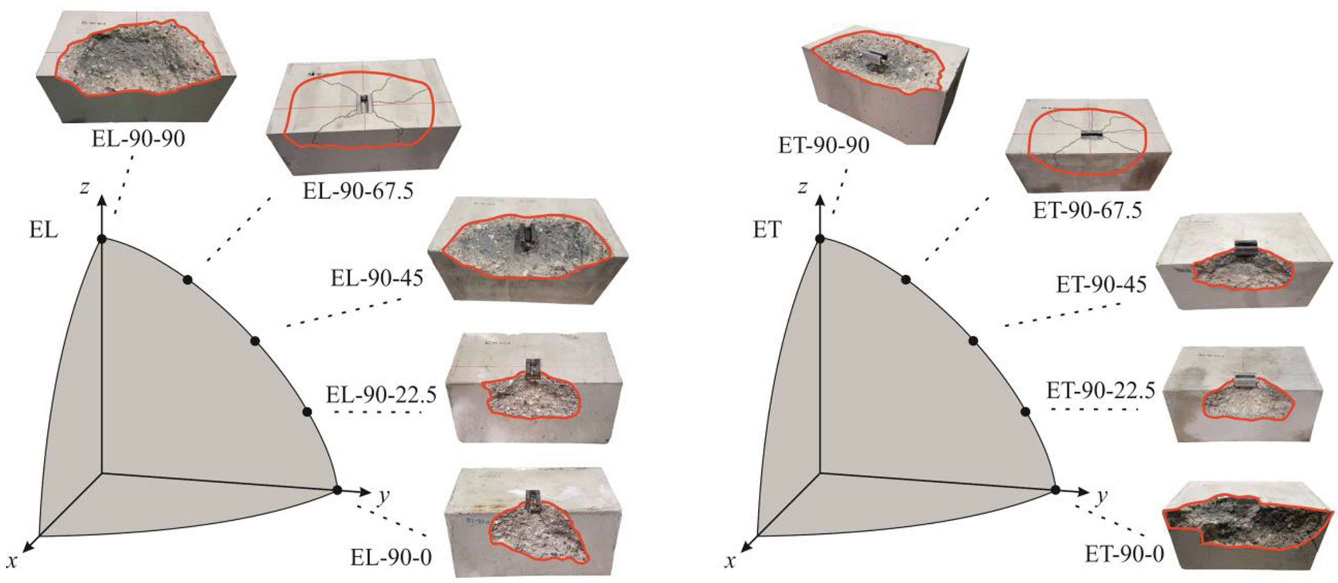

FIGURE 9 Concrete failure of test bodies in edge configurations EL and ET

Due to the short edge distances of the anchor, the concrete cone forms only partially. With higher tension cracking shifts from the side to the top face. This holds true for both, edge and corner configurations.

In comparison of the longitudinal and transverse edge configurations the results for a vertical loading angle of $\beta = 45°$ are most interesting (Figure 9). If the anchor channel is longitudinally mounted (EL), the failure mode is dominated by tension in direction of the upper surface. By contrast, if an anchor channel is mounted transverse (ET), failure tends to happen toward the edge. Despite equivalent edge distances of the anchor and equal ultimate load levels in both cases different failure modes occur.

Moreover, with flat load angles (0°), it is realized that transverse mounted anchor channels (ET) activate a greater region of concrete. Compared with a longitudinal configuration (EL) in which the load is merely induced by the anchor (due to a smaller cross-section), the channel in transverse configuration induces the load by the channel profile. Through the significantly greater area (85-mm wide, 34-mm high) much more concrete is activated.

The results of the corner tests (Figure 10) show not only differences for varying vertical angles, but also an influence of the horizontal load angle α. Especially in the xy base plane ($\beta = 0°$), it can be seen that the breakout is much more pronounced in loading direction than on the lateral surface parallel to it. In this basic plane, the breakout body in Figure 10 changes accordingly from the left side surface (C-0-0) over the corner (C-45-0) to the right side surface (C-90-0).

4.2 | Failure loads

Since the test program was carried out in two series over several days each, the maximum load-bearing capacities determined in the test must be normalized with respect to the compressive strength of concrete to obtain comparable results. For this purpose, the strength was determined on each test day (see Tables 3 and 4). The normalization of the maximum test loads $F_{\max}$ is carried out via the root relationship of the compressive strength according to Equation (4)[13] related to the average strength of 27.6 N/mm^2.

$$\overline{F}_{\max} = F_{\max} \cdot \sqrt{\frac{f_{\mathrm{cm,test}}}{27.6\,\mathrm{N/mm^2}}} \tag{4}$$

Tables 3 and 4 summarize the normalized results for all tests performed. For the not-tested configurations C-22.5-67.5 and C-67.5-67.5, the results were interpolated from C-0-67.5 and C-45-67.5 or C-45-67.5 and C-90-67.5, respectively. Additionally, the horizontal (V) and vertical (N) components of the mean maximum load $\overline{F}_{\max,m}$ are listed for all configurations.

5 | ANALYSIS AND DISCUSSION OF THE RESULTS

At first glance, for all configurations (E and C), it is noticeable that the load capacities are larger for higher load angles ($\beta = 67.5°$ or 90°) than for smaller ones

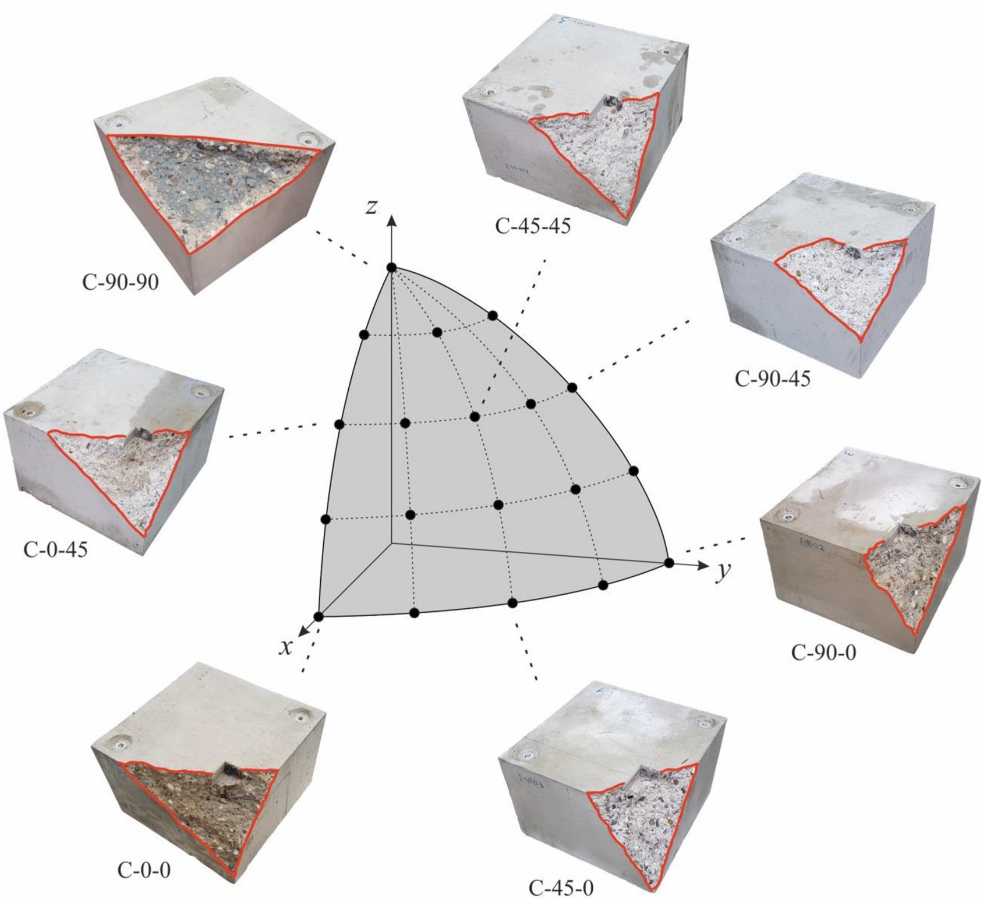

FIGURE 10 Concrete failure of test bodies in corner configurations (C)

($\beta = 0°$). For flat to medium angles ($\beta = 22.5°$ or $45°$), it is noticeable that the load-bearing capacities are mostly lower than in the principal axis direction ($\beta = 0°$ and $90°$). On the basis of the raw data, interaction in the form of reduced load-bearing capacities can thus already be recognized if tensile loads occur in addition to horizontal loads. This applies to both the edge and the corner tests.

This interaction is investigated by regression analysis of the test data, which provides optimal functions in the linear-least-squares sense that capture the influence on the load-bearing capacity of anchor channels under multiaxial tensile loading. The evaluation of the interaction is done for each configuration separately employing the mean results $\overline{F}_{\max,m}$ according to Tables 3 and 4.

Subsequently, a uniform interaction function is searched for, which captures all data (and thus all investigated angles) of the corner configuration at once. With this function, the bearing capacities under inclined loads can then be calculated directly from those in the principal axis direction while multiaxial loading is covered. This is advantageous since in practice, bearing capacities in the principal axis direction are often already known (by calculation) or can be determined easily from just few tests.

5.1 | Alternative regression functions to capture interaction

For evaluation of the experimental data, generalized Lamè curves (Equation (5)) and a trilinear approach (Equation (6)) were used as regression functions. Such types of functions are known to engineers working in concrete construction, for example, from the interaction of shear and torsion, and represent a generalized form of relations already introduced by Wohlfahrt[8] and by Oluokon and Burdette[11] for anchor channels under biaxial loading. The most recent specification in EN 1992-4[13] also bases on them. Figure 11 exemplifies these curves employing their parameters a, b, and c so that the impact of these can be visually assessed. (Multiple) linear regression delivers the optimal parameter set to best fit the test data in a least squares sense.

$$\left(\frac{V}{V_{\max}}\right) + \left(\frac{N}{N_{\max}}\right) \leq a \text{ with } a \geq 1.0 \tag{5}$$

$$\left(\frac{V}{V_{\max}}\right)^b + \left(\frac{N}{N_{\max}}\right)^c \leq 1{,}0 \text{ with } b, c \geq 0 \text{ and } V \leq V_{\max} \text{ and } N \leq N_{\max} \tag{6}$$

Generalized Lamè curves are characterized by two independent parameters, b and c, which are exponents of

TABLE 3 Experimental results of the edge configurations

Edge configuration	No. of tests	$f_{c,cube}$ [N/mm^2]	$\overline{F}_{max,1}$ [kN]	$\overline{F}_{max,2}$ [kN]	$\overline{F}_{max,3}$ [kN]	$\overline{F}_{max,4}$ [kN]	$\overline{F}_{max,m}$ [kN]	$\overline{F}_{max,m,V}$ [kN]	$\overline{F}_{max,m,N}$ [kN]
EL-90-0	2	30.1	30.5	31.2	—		30.9	30.9	0
EL-90-22.5	2	27.2	28.4	28.6	—		28.5	26.3	10.9
EL-90-45	2	28.7/27.2	29.3	28.0	—		28.6	20.2	20.2
EL-90-67.5	2	27.2	34.7	33.2	—		34.0	13.0	31.4
EL-90-90	3	28.6/27.2	46.7	46.7	45.6		46.4	0	46.4
ET-90-0	2	30.1	30.9	31.1	—		31.0	31.0	0
ET-90-22.5	2	27.2	30.1	29.8	—		30.0	27.7	11.5
ET-90-45	4	28.7/27.2	25.5	26.7	33.3	30.1	28.9	20.4	20.4
ET-90-67.5	2	27.2	37.2	35.6	—		36.4	13.9	33.6
ET-90-90	2	28.6	43.1	41.5	—		42.3	0	42.3

TABLE 4 Experimental results of the corner configurations

Corner configuration	No. of tests	$f_{c,cube}$ [N/mm^2]	$\overline{F}_{max,1}$ [kN]	$\overline{F}_{max,2}$ [kN]	$\overline{F}_{max,3}$ [kN]	$\overline{F}_{max,m}$ [kN]	$\overline{F}_{max,m,V}$ [kN]	$\overline{F}_{max,m,N}$ [kN]
C-0-0	2	28.5	25.7	26.3	—	26.0	26.0	0
C-0-22.5	2	27.3	22.1	22.6	—	22.3	20.6	8.5
C-0-45	2	28.7	22.9	22.9	—	22.9	16.2	16.2
C-0-67.5	2	28.4	29.5	27.6	—	28.5	10.9	26.3
C-22.5-0	2	26.7	21.9	20.0	—	21.0	21.0	0
C-22.5-22.5	2	27.3	21.6	20.4	—	21.0	19.4	8.0
C-22.5-45	2	26.7	20.8	24.2	—	22.5	15.9	15.9
C-22.5-67.5	[a]	—	—	—	—	28.2	10.8	26.1
C-45-0	3	30.1	21.5	26.4	20.7	22.9	22.9	0
C-45-22.5	2	27.3	19.0	18.1	—	18.6	17.2	7.1
C-45-45	2	28.7	23.3	20.7	—	22.0	15.6	15.6
C-45-67.5	2	28.4	29.1	26.9	—	28.0	10.7	25.9
C-67.5-0	2	26.7	22.0	19.5	—	20.8	20.8	0
C-67.5-22.5	2	27.3	18.5	18.1	—	18.3	16.9	7.0
C-67.5-45	2	26.7	24.2	22.7	—	23.4	16.5	16.5
C-67.5-67.5	[a]	—	—	—	—	29.0	11.1	26.8
C-90-0	2	30.1	19.7	21.5	—	20.6	20.6	0
C-90-22.5	2	27.2	20.6	21.3	—	21.0	19.4	8.0
C-90-45	2	28.7	23.8	21.5	—	22.7	16.1	16.1
C-90-67.5	2	28.4	30.4	29.2	—	29.8	11.4	27.5
C-90-90	3	28.6	37.9	38.2	41.2	39.1	0	39.1

[a]Interpolated.

the two summands (Equation (6)). These two parameters must be greater than zero, but can otherwise be freely selected. A choice of $b = c$ leads back to the original Lamè curve with just one exponential parameter. With $b = c = 2$ one obtains an ordinary ellipse. If one additionally chooses $V_{max} = N_{max}$ the curve becomes a circle with the radius V_{max} or N_{max}, respectively. Other choices yield concave or convex curves and also curves

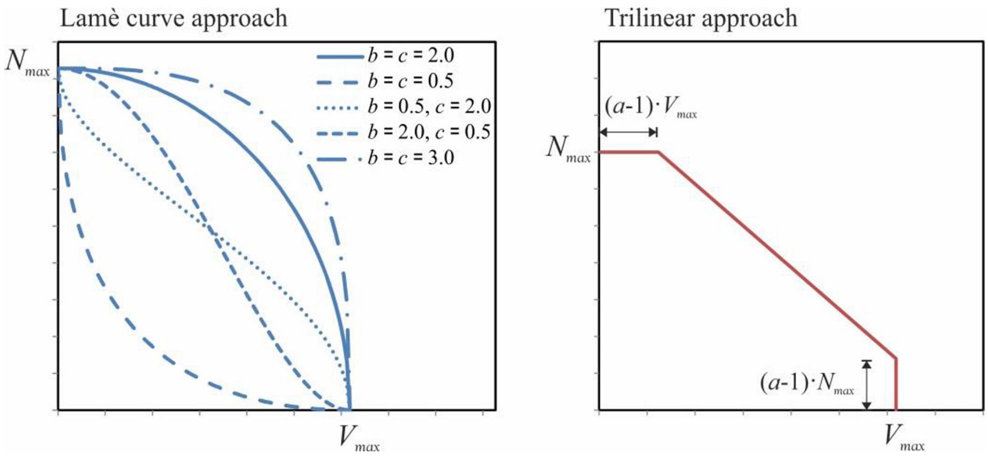

FIGURE 11 Impact of parameters in the alternative regression functions (left: Lamè curves; right: trilinear approach)

with inflection points. In general Lamè curves are quite flexible. They can also be linear if $b = c = 1$. The result is a straight line which coincides with the trilinear approach and a parameter $a = 1$.

In particular, the parameter a in the trilinear approach decides on the kinks of the curve. Physically, one load component can be increased up to that kink while a reduction of the other component must not be expected.

The regression functions are obtained by rearranging Equations 5 and 6 in such a way that the bearable force N can be calculated as a function of the variable V.

$$\text{Lamè curve approach}: \widehat{N}(V) = \left(1.0 - \left(\frac{V}{V_{\max}}\right)^b\right)^{1/c} \cdot N_{\max} \quad (7)$$

$$\text{Trilinear approach}: \widehat{N}(V) = \left(a - \frac{V}{V_{\max}}\right) \cdot N_{\max} \quad (8)$$

For these functions the optimum set of parameters a or b and c that best fits the test data in a least squares sense is found by (multiple) linear regression. To minimize computational effort, the ranges of all three parameters were restricted ($a \in [1,2[$; $b \in]0,3]$; $c \in]0,3]$). In the trilinear approach this ensures that always one inclined branch and two plateaus form. In the limit case $a = 2$ a rectangle is obtained. As long as $b = c$ for the Lamè approach, no turning points occur. They occur if one parameter is greater than zero while the other is smaller than zero. For ($b = c < 2$) hypo elliptical or with ($b = c > 2$) hyper elliptical shapes form.

Within these limits, the parameters are regularly generated and combined with each other and the corresponding regression function is determined. For each realization a different fit results, which can be evaluated against the alternatives via its coefficient of determination. The best fit has the highest coefficient of determination R^2 or R^2_{adj}. Both are measures of linear regression, which indicate how well an independent variable (here: V) is suited to explain the variance of a dependent variable (here: N). $R = 1$ denotes a perfect match or functional dependence. Then, the portion of unexplained variation in the total variation is zero. The coefficient of determination R^2 is calculated according to Equation (9):

$$0 \le R^2 = \frac{\sum\left(\widehat{N}_i - \overline{N}\right)^2}{\sum\left(N_i - \overline{N}\right)^2} = 1 - \frac{\sum\left(N_i - \widehat{N}_i\right)^2}{\sum\left(N_i - \overline{N}\right)^2} \le 1 \quad (9)$$

Therein, $\widehat{N}_i$ corresponds to the value of the regression function $\widehat{N}(V_i)$ according to Equations (7) or (8), $\overline{N}$ denotes the empirical mean, and N_i the measured value of the ith tensile force from Tables 3 or 4 ($=\overline{F}_{\max,m,N}$), respectively. For the computation of R^2, the five related data points of a configuration (or a meridian) are used ($n = i = 5$). But, only the three central data points ($\beta = 22.5°/45°/67.5°$) might impair the model quality. Just for these a deviation between the experimental N_i and the predicted quantity $\widehat{N}_i$ is possible. At the main axes ($\beta = 0°/90°$) prediction and experimental result must exactly coincide $\left(N_i = \widehat{N}_i\right)$. This holds true for both the trilinear and the Lamé approach.

To avoid overfitting, the adjusted counterpart according to Equation (10) is used for the evaluation instead of the coefficient of determination according to Equation (9) throughout. The adjusted value is calculated from the coefficient of determination and additionally takes into account the numbers of data points (n) and independent parameters a ($k = 1$) or b and c ($k = 2$) when determining the regression function.

TABLE 5 Best fit results from regression analysis

	#1 trilinear		#2 Lamè curve		
Configuration	***a***	R^2_{adj}	***b***	***c***	R^2_{adj}
EL-90-β	1.09	0.9998	1.08	1.25	0.9993
ET-90-β	1.18	0.9880	1.43	1.33	0.9773
C-0-β	1.05	0.9927	1.5	0.79	0.9993
C-22.5-β	1.16	0.9974	1.14	1.52	0.9987
C-45-β	1.05	0.9575	2.31	0.49	0.9810
C-67.5-β	1.14	0.9320	2.16	0.82	0.9253
C-90-β	1.20	0.9869	1.47	1.44	0.9938

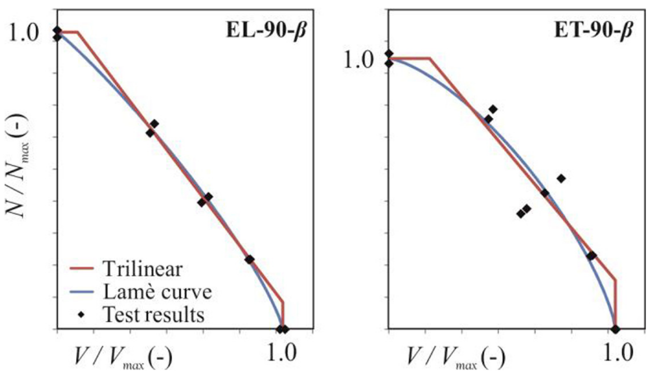

FIGURE 12 Best fits from regression for configurations EL-90-β and ET-90-β (#1 and #2)

$$R^2_{adj} = 1 - \left[\frac{(1-R^2)(n-1)}{n-k-1}\right] \tag{10}$$

5.2 | Evaluation of the interaction tests on anchor channels

Table 5 summarizes the parameters of the best fits of all cases investigated. They are shown separately for the edge and corner configurations in Figures 12 and 13.

Overall, both the trilinear and the Lamè approach capture the test results in great agreement (R^2_{adj} always close to 1). However, the best fit parameters differ depending on the horizontal load direction with respect to the channel axis (longitudinal or transverse loading).

In general, larger interaction is observed in case of combined tensile and longitudinal stressing than with tensile and transverse stressing. This is seen from comparison of the edge configurations (EL to ET), as well as of the corner configurations (C; in particular comparing the 0° and 90° meridians). Larger interaction in the Lamè approach is associated with a flatter curve that comes along with smaller exponents, b and c. For the trilinear approach interaction is more pronounced the lower a is which simultaneously determines the position of the two kinks of the curve.

A potential reason for the greater interaction in case of combined tensile and longitudinal stressing is seen in the

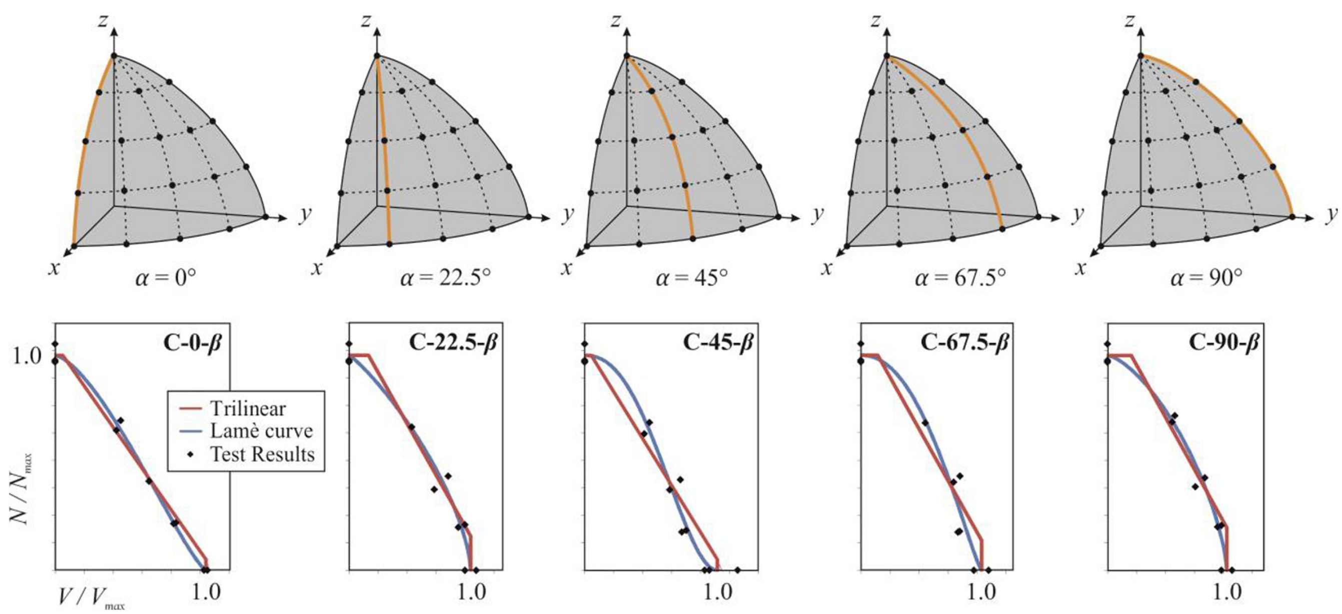

FIGURE 13 Best fits from regression for corner configurations (#1 and #2)

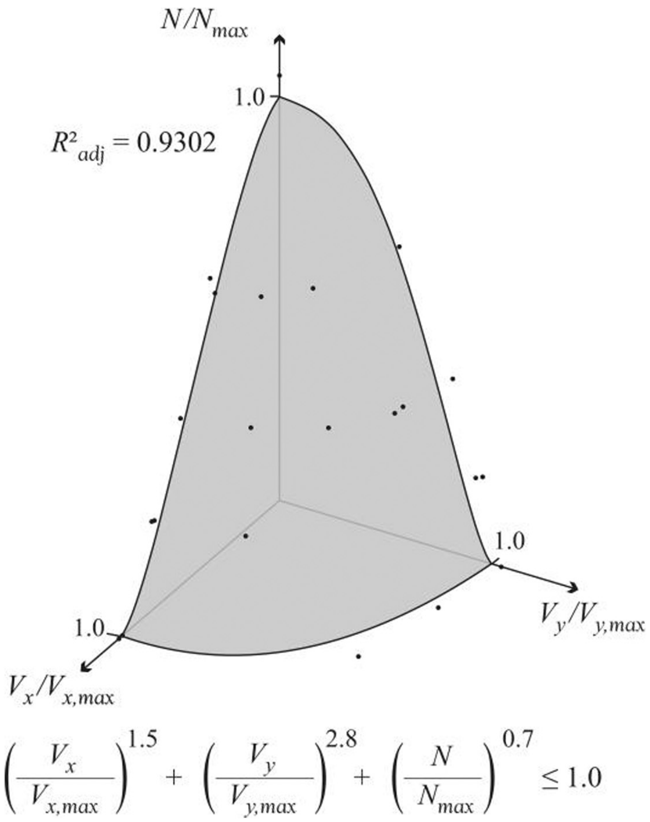

FIGURE 14 Best fit from regression for corner configuration—3D Lamè approach

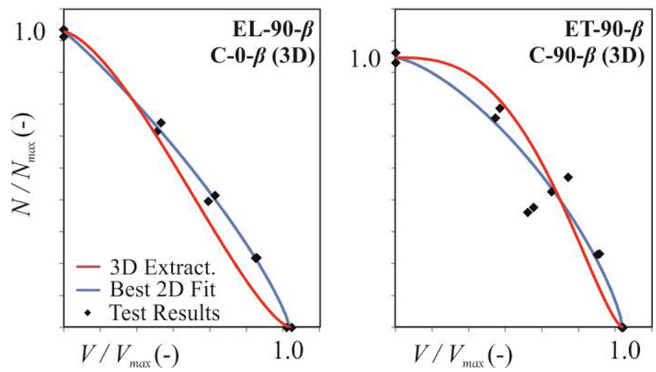

FIGURE 15 Comparison of best 2D fit and 3D extraction

elimination of friction and adhesion between the anchor channel and the surrounding concrete, which is induced by slight lifting of the channel during tensile loading. As both effects contribute to a certain extent to the load introduction into the concrete in the case of pure longitudinal stressing their proportion is minimized by the additional tensile component. Consequently, the tensile loads and the longitudinal stresses are both mainly transferred via the anchor and thus cause stress concentration there.

In contrast the load components are transferred to the concrete at different places in the case of combined tensile and transverse stressing. While the tensile forces are transferred directly at the anchor, the transversal component is induced by the lips of the anchor channel.[31] Thus, no stress concentrations occur and interaction is lower.

Comparing the results with the current regulations in EN 1992-4[13] and AC232,[14] it is noticeable that the interactions provided there were presumably derived from tests with combined tensile transverse stressing. This impression originates from the exponents, which are much more consistent then. Especially these exponents ($b = c = 1.5$ in EN 1992-4, or 5/3 in AC232), are in good agreement with the test results for both the ET configuration and the C-90° meridian of the corner tests.

In addition to the 2D evaluations of longitudes, an overall 3D fit can also be determined for the corner configuration. To determine the best fit, the above introduced functions have been extended by a third term to cover the third dimension. Since for the trilinear approach a clearly worse model quality is gained, just the Lamè approach is treated in the remainder[32]:

$$\left(\frac{V_x}{V_{x,\max}}\right)^d + \left(\frac{V_y}{V_{y,\max}}\right)^e + \left(\frac{N}{N_{\max}}\right)^f \leq 1,0 \qquad (11)$$

Then, the resulting shape is a superellipsoid. The best fit from regression is shown along with the three exponents and the coefficient of determination in Figure 14.

Although a general fit is consistently found it does not have the quality of the 2D fits for most meridians. The regression functions of the individual meridians are quite different, as shown in Table 5 and Figure 13, but must all be considered for the holistic interaction surface. Although this compromise results in a lower coefficient of determination, it is still practically usable and of acceptable quality.

In principle, this 3D fit can also be used to represent plane interactions by deleting the unnecessary term in the equation. However, due to the tradeoff character of the uniform solution, this results in lower measures of determination. When the 2D solutions were extracted from the 3D case (by deleting unnecessary terms), the following coefficients of determination are gained:

$$\text{EL}: \left(\frac{V}{V_{\max}}\right)^{1.5} + \left(\frac{N}{N_{\max}}\right)^{0.7} \leq 1.0 => R^2_{\text{adj}} = 0.9080$$

$$\text{ET}: \left(\frac{V}{V_{\max}}\right)^{2.8} + \left(\frac{N}{N_{\max}}\right)^{0.7} \leq 1.0 => R^2_{\text{adj}} = 0.9133$$

These are significantly lower than for the best 2D fit according to Table 5 (EL: 0.9993, ET: 0.9773). Both the best 2D fit and the 3D extraction are shown in Figure 15 for comparison. Nevertheless, the uniform 3D approach is easy and accurate for practical needs. However, if one restricts oneself to plane interaction the results for EL and ET according to Table 5 should be used instead since they deliver the most realistic prediction of interaction.

6 | CONCLUSIONS

The two dimensional rotational capability of the developed test rig has been proven to enable testing of arbitrary 3D load interaction on anchor channels embedded in concrete. Its functionality and variability seems promising to allow testing of dowels and anchors in the future.

In particular minimization of specimen dimensions ensures its economy and reduces the effort regarding production, storage, transport and testing. Minimization turns out as a trade-off between space the breakout body needs to form unimpaired on the specimen's surface and the dimensions required from its design against the test loads. The assumptions made in Equations (1)–(3) and Figure 4 regarding the size of the breakout body have been proven being accurate for anchor channels.

Dependent on the direction of loading interaction shows disparately. In general, interaction is more pronounced in combined tensile and longitudinal stressing than in combined tensile and transversal stressing. Also the crack patterns are shown to be influenced by the direction of loading, for both horizontal and vertical loads.

In most cases, trilinear approaches and Lame curves perform equally well in capturing load interaction mathematically. Just in the 3D case Lame curves are better. In case of plane load interaction the derived 2D relations are recommended to gain most realistic predictions.

So far, it remains unresolved to what extent interaction impairs the capacity for very small and large angles in the constant branches of the trilinear approach. Such angles have not been considered here. Moreover, an influence of the type of anchor channel, due to its different dimensions, remains unclear and needs further investigation. Also longer channels with more anchors should be tested. Neighboring anchors might alter the bearing capacity of the channel subjected to 3D loading.

ACKNOWLEDGMENTS

Open Access funding enabled and organized by Projekt DEAL.

DATA AVAILABILITY STATEMENT

The data that support the findings of this study are available from the corresponding author upon reasonable request.

ORCID

Dustin Konertz https://orcid.org/0000-0002-3236-1885

REFERENCES

1. Bokor B, Sharma A, Hofmann J. Concrete edge failure of anchor groups placed parallel to an edge. ACI Struct J. 2021;118(2):237–48.
2. Spyridis P. Fastening technology as an interface and integration element of architectural, structural, and building engineering. In: 4th international conference on structures and architecture (ICSA), Lisbon; 2019.
3. Mahrenholtz C, Sharma A, Kucharski M, Eligehausen R, Hammill NL, Hastings B. Anchor reinforcement for anchor channels. Concr Int. 2021;43(9):24–9.
4. Dubai SI. Construction Update [Internet]. 2007. [cited 2022 Apr 18]. Available from: https://commons.wikimedia.org/w/index.php?curid=3201302
5. Konertz D, Kocur GK, Clauß F, Häusler F, Mark P. Anchor channels under 3D-load interaction: new approaches to load distribution and design. In: Derkowski W et al., editors. Concrete: innovations in materials, design and structures, fib syposium 2019. Poland: Krakow; 2019. p. 635–42.
6. Fuchs W, Eligehausen R, Breen JE. Concrete capacity design (CCD) approach for fastening in concrete. ACI Struct J. 1995;92(1):73–93.
7. Grosser P, Eligehausen R, Ozbolt J. 3D FE analysis of anchor channels and headed anchors under shear load close to the edge. In: Oh BH et al., (editors). Fracture mechanics of concrete and concrete structures: recent advances in fracture mechanics of concrete. London: Taylor & Francis; 2010. p. 560–7.
8. Wohlfahrt R. Tragverhalten von Ankerschienen ohne Rückhängebewehrung (load bearing behaviour of anchor channels without supplementary reinforcement). Dissertation, University of Stuttgart, Stuttgart, Germany; 1996 [in German].
9. Schmidt T. Tragverhalten von Ankerschienen unter Querlast in Schienenlängsrichtung (load bearing behavior of anchor channels under shear load acting in the longitudinal direction of the channel axis). Dissertation, University of Stuttgart, Stuttgart, Germany; 2017 [in German].
10. Kraus J. Tragverhalten und Bemessung von Ankerschienen unter zentrischer Zugbelastung (Load bearing behavior and design of channel bars under centric tension loads). Dissertation, University of Stuttgart, Stuttgart, Germany; 2003 [in German].
11. Oluokon FA, Burdette EG. Behavior of channel anchors in thin slabs under combined shear and tension (pullout) loads. ACI Struct J. 1993;90(4):407–13.
12. American Concrete Institute (ACI). Building code requirements for structural concrete (ACI 318-19): An ACI standard: commentary on building code requirements for structural concrete (ACI 318R-19). Farmington Hills: American Concrete Institute; 2019.
13. European Committee for Standardization (CEN). EN 1992-4: 2018—Eurocode 2: Design of concrete structures—Part 4: Design of fastenings for use in concrete; 2018.
14. International Code Council-Evaluation Service (ICC-ES). AC232: acceptance criteria for anchor channels in concrete elements. Whittier: ICC-ES; 2019.

15. European Committee for Standardization (CEN) CEN/TR 17080: Design of fastenings for use in concrete—anchor channels—supplementary rules; 2018.
16. Fuchs W, Eligehausen R, Hofmann J. EN1992-4: The long route to a European standard for fastening to concrete. In: Sharma A, Hofmann J, (editors). 3rd international symposium on connections between steel and concrete; September 27–29, 2017. Stuttgart, Germany: Institute of Construction Materials, University of Stuttgart; 2017.
17. Mahrenholtz C, Sharma A. Qualification and design of anchor channels with channel bolts according to the new EN 1992-4 and ACI 318. Struct Concr. 2019;21(1):1–13. https://doi.org/10.1002/suco.201800341
18. Eligehausen R, Mallée R, Silva JF. Anchorage in concrete construction. Berlin, Germany: Ernst und Sohn; 2006.
19. Potthoff M. Tragverhalten und Bemessung von Ankerschienen unter Querbelastung (Load behaviour and design of channel bars under shear load). Dissertation, University of Stuttgart, Stuttgart, Germany; 2008 [in German].
20. Schmidt T, Hofmann J. Anchor channels under shear load acting in the longitudinal direction of the channel axis. In: Sharma A, Hofmann J, (editors). Proceedings of the 3rd international symposium on connections between steel and concrete. Stuttgart, Germany: Institute of Construction Materials, University of Stuttgart; 2017. p. 480–8.
21. Konertz D, Kocur GK, Häusler F, Mark P. Longitudinal shear transmission of anchor channels into concrete—an experimental approach. Struct Concr. 2021;22(2):1072–84. https://doi.org/10.1002/suco.202000133
22. Konertz D, Löschmann J, Clauß F, Mark P. Fiber optic sensing of strain and temperature fields. Bauingenieur. 2019;94(7/8):292–300. [in German].
23. Konertz D, Mahrenholtz C, Mark P. Verification of a load distribution model for anchor channels in the experimental virtual lab. In: Proceedings on concrete 2019: concrete in practice—progress through knowledge, Sydney; 2019.
24. European Organisation for Technical Assessment (EOTA). European assessment document EAD 330008-02-0601. Anchor Channels; Brussels: EOTA; 2016.
25. Putke T, Bohun R, Mark P. Experimental analyses of an optimized shear load transfer in the circumferential joints of concrete segmental linings. Struct Concr. 2015;16(4):572–82.
26. Bocklenberg L, Mark P. Thick slab punching with symmetry reductions. Struct Concr. 2020;21(3):1–15. https://doi.org/10.1002/suco.201900480
27. Bocklenberg L, Winkler K, Mark P, Rybarz S. Low friction sliding planes of greased ptfe for high contact pressures. Open J Civ Eng. 2016;6(2):105–16.
28. Clauß F, Ahrens MA, Mark P. A comparative evaluation of strain measurement techniques in reinforced concrete structures—a discussion of assembly, application and accuracy. Struct Concr. 2021;22(5):2992–3007. https://doi.org/10.1002/suco.202000706
29. Petraroia DN, Mark P. Variable, full-scale tester for tunnel linings. Struct Concr. 2021;22(6):3353–67. https://doi.org/10.1002/suco.202000806
30. Mark P. Shear-resistant design of biaxially loaded RC beams. Mag Concr Res. 2007;59(1):21–8. https://doi.org/10.1680/macr.2007.59.1.21
31. Federation International du Bèton (fib). Design of anchorages in concrete—guide to good practice. Lausanne, Switzerland: fib; 2011.
32. Konertz D. Tragverhalten räumlich beanspruchter Ankerschienen (load-bearing behavior of spatially stressed anchor channels). Dissertation, Ruhr University Bochum, Bochum, Germany; 2021 [in German].

AUTHOR BIOGRAPHIES

Dustin Konertz, Institute of Concrete Structures, Ruhr University Bochum, Universitätstr. 150, 44801 Bochum, Germany
dustin.konertz@rub.de

Christoph Mahrenholtz, Jordahl GmbH, Head of Engineering, Berlin, Germany
christoph.mahrenholtz@pohlcon.com

Peter Mark, Institute of Concrete Structures, Ruhr University Bochum, Universitätstr. 150, 44801 Bochum, Germany
peter.mark@rub.de

How to cite this article: Konertz D, Mahrenholtz C, Mark P. Three-dimensional testing of fasteners. Structural Concrete. 2023;24(2):2623–37. https://doi.org/10.1002/suco.202200387